ADVANCED FUNCTIONAL MATERIALS
www.afm-journal.de

Engineering of Facets, Band Structure, and Gas-Sensing Properties of Hierarchical Sn^{2+}-Doped SnO_2 Nanostructures

Hongkang Wang, Kunpeng Dou, Wey Yang Teoh, Yawen Zhan, Tak Fu Hung, Feihu Zhang, Jiaqiang Xu, Ruiqin Zhang, and Andrey L. Rogach**

Hierarchical SnO_2 nanoflowers, assembled from single-crystalline SnO_2 nanosheets with high-index (11$\bar{3}$) and (10$\bar{2}$) facets exposed, are prepared via a hydrothermal method using sodium fluoride as the morphology controlling agent. Formation of the 3D hierarchical architecture comprising of SnO_2 nanosheets takes place via Ostwald ripening mechanism, with the growth orientation regulated by the adsorbate fluorine species. The use of Sn(II) precursor results in simultaneous Sn^{2+} self-doping of SnO_2 nanoflowers with tunable oxygen vacancy bandgap states. The latter further results in the shifting of semiconductor Fermi levels and extended absorption in the visible spectral range. With increased density of states of Sn^{2+}-doped SnO_2 selective facets, this gives rise to enhanced interfacial charge transfer, that is, high sensing response, and selectivity towards oxidizing NO_2 gas. The better gas sensing performance over (10$\bar{2}$) compared to (11$\bar{3}$) faceted SnO_2 nanostructures is elucidated by surface energetic calculations and Bader analyses. This work highlights the possibility of simultaneous engineering of surface energetics and electronic properties of SnO_2 based materials.

1. Introduction

Metal oxide nanostructures with well-defined morphologies and highly reactive surfaces have attracted intense research interest due to their shape, size, and surface dependent properties.[3] Much of the core of such work is built on the understanding of crystal facets growth and control, including their stability and reactivity.[1] In particular, studies of facets control have been not only crucial for their synthesis but also for tuning the chemical and physical properties.[2] Surfaces with high reactivity usually diminish rapidly during crystal growth to minimize total surface energy. As such, the reliable synthesis of nanostructures with controllable crystallographic facets remains the bottleneck in materials chemistry.[2b] The ability to extend both morphological and facets control over oxide semiconductors influence directly their electronic and physicochemical behavior. This in turn offers interesting applications in fields such as gas sensing, photocatalysis, photovoltaics, energy storage, and biodiagnostics.

Like a handful of other oxide semiconductors, SnO_2 is a robust material that can be made as 0D nanoparticles,[4] 1D nanorods,[5] nanowires[6] and nanotubes,[7] 2D nanosheets,[8] and 3D hierarchical architectures with hollow or mesoporous structures.[9] Among these different morphologies, the 3D hierarchical nanostructures, normally constructed by self-assembly, offer interesting physical and chemical properties.[9d,10] In general, self-assembly involves almost in a simultaneous fashion, the interactions of van de Waals forces, hydrogen bonding, ionic interactions, hydrophilicity/hydrophobicity and covalent bonding.[10a,11] One particularly important aspect of the self-assembly approach in relation to tailored synthesis of metal oxide nanostructures is the realization of highly reactive surfaces through specifically exposed crystallographic facets. Considerable efforts have been devoted to provide both kinetic and thermodynamic control by changing the relative stabilities of different crystal facets with foreign adsorbate species.[2b,13] In particular, remarkable progress has been achieved in the synthesis of anatase TiO_2 single crystals, where high percentage of reactive (001) facets exposed can be achieved through surface fluorine passivation.[2b,14] In the case of SnO_2, crystals are usually enclosed by (110), (101), or (100) low energy facets,[1d] while for octahedral SnO_2 nanoparticles (221) high energy facets have been reported.[13]

The applicability of SnO_2 as gas sensor is a highly important one where high energy facets can in principle affect the sensitivity of the device. The gas sensing is based on a significant electrical resistance change upon chemisorption of analyte

H. K. Wang, Dr. K. P. Dou, Y. W. Zhan, T. F. Hung, Prof. R. Q. Zhang, Prof. A. L. Rogach
Department of Physics and Materials Science
& Centre for Functional Photonics (CFP)
City University of Hong Kong, Hong Kong SAR
E-mail: aprqz@cityu.edu.hk; andrey.rogach@cityu.edu.hk
Dr. W. Y. Teoh
Clean Energy and Nanotechnology (CLEAN) Laboratory
School of Energy and Environment
City University of Hong Kong, Hong Kong SAR
F. H. Zhang, Prof. J. Q. Xu
Department of Chemistry
College of Science
Shanghai University
Shanghai 200444, P. R. China

DOI: 10.1002/adfm.201300303

molecules on an oxide semiconductor. For n-type SnO_2, an electron-depletion layer forms on the semiconductor surface due to chemisorbed oxygen.[13,15] The oxidative or reductive interactions between the surface oxygen and the target gas result in a change in the electrical conductivity in proportion to the gas concentration. The gas sensitivity increases rapidly when the dimensions of oxide sensing materials become comparable to the typical thickness of the electron depletion layer near the surface.

Herein, we report the synthesis of 3D hierarchical SnO_2 nanoflowers assembled from $(11\bar{3})$ or $(10\bar{2})$ faceted 2D nanosheets (denoted as $(11\bar{3})$-SnO_2 and $(10\bar{2})$-SnO_2, respectively) through hydrothermal treatment of tin(II) precursor and using sodium fluoride as the morphology controlling agent. As we show in this work, fluorine ions influence surface energy of the crystal nuclei, by which the growth orientation of 2D SnO_2 nanosheets can be controlled by adjusting the ratio of fluorine to tin precursor. We also show how the use of Sn(II) precursor results in a simultaneous Sn^{2+} self-doping of SnO_2 nanostructures, leading to the formation of tunable oxygen vacancy bandgap states and the corresponding shifting in the semiconductor Fermi levels. Combined with the facets control, the increased density of states gives rise to enhanced charge transfer responsible for the sensing of oxidizing gas NO_2. Our work highlights the possibility of simultaneous engineering of surface energetics and electronic properties of SnO_2 based nanostructures.

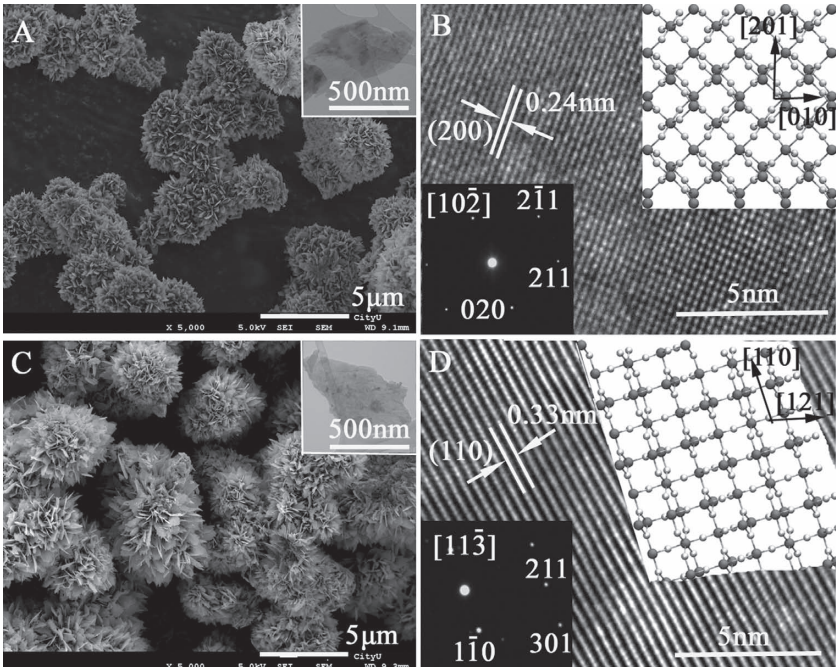

Figure 1. Hierarchical SnO_2 nanoflowers with exposed A,B) $(10\bar{2})$ and C,D) $(11\bar{3})$ facets. Images (A,C) show the SEM with insets of TEM of the nanosheets. Images (B,D) show the HRTEM of the nanosheets and the respective fast Fourier-transform patterns (insets), as well as the schematic illustration of the atomic planes (large grey spheres: Sn atoms, small white spheres: O atoms).

2. Results and Discussion

The synthesis of hierarchical Sn^{2+} self-doped SnO_2 nanostructures resembling peony flowers in their appearance has been accomplished via a hydrothermal oxidation of Sn^{2+} (employing $SnCl_2 \cdot 2H_2O$ as a precursor) and using NaF as the shape-controlling agent (**Figure 1**). Under hydrothermal conditions, a significant fraction of the Sn^{2+} is easily oxidized to Sn^{4+} in the presence of water and dissolved oxygen,[9d] and hence SnO_2 rather than SnO nanostructures are obtained. The resultant nanoflowers are formed from the self-assembly of edgy petal-shaped nanosheets, which preferential facets can be easily tuned during the synthesis. We demonstrate here that by controlling the amount of NaF, and hence the ratio of F to Sn ($R_{F/Sn}$) from 3.0 to 4.8, it is possible to obtain SnO_2 nanosheets with predominant $(11\bar{3})$ (Figure 1C,D) and $(10\bar{2})$ facets (Figure 1A,B), respectively. As references, undoped hierarchical SnO_2 nanostructures composed of fan-shaped nanosheets assembled into hollow spheres were obtained when using conventional $SnCl_4 \cdot 5H_2O$ as the Sn^{4+} precursor,[16] while only irregular nanoparticles were obtained when using $SnCl_2 \cdot 2H_2O$ and $SnCl_4 \cdot 5H_2O$ alone, i.e., in the absence of NaF directing agent. Fluoride ions such as those from NaF or those from yet other precursors such as HF and NH_4F are known to preserve high-energy facets in other metal oxide systems, such as TiO_2,[2b] through selective capping. We have studied the influence of the amount of fluorine in details, and did not find the formation of hierarchical SnO_2 nanoflowers for $R_{F/Sn}$ lower than 1. Sufficient amount of NaF ($R_{F/Sn} > 3$) was necessary to prevent the aqueous hydrolysis of $SnCl_2 \cdot 2H_2O$.

As we further reveal through first principles density functional theory (DFT) calculations (**Table 1**), fluoride capping lowers the surface energies, γ, of these high index facets significantly, much more so than that of the low index facets, i.e., (001) and (011) facets. Two sets of pseudopotential configurations were adopted: (i) $5s^2 4d^{10} 5p^2$ electrons for Sn and $2s^2 2p^4$ for O, $2s^2 2p^5$ for F, and (ii) $5s^2 5p^2$ for Sn, $2s^2 2p^4$ for O and $2s^2 2p^5$ for F. Similar results were obtained for both similar

Table 1. Surface free energies (γ) for four different SnO_2 crystal facets–clean as well as terminated by F atoms–calculated using two sets of pseudopotential configurations, as specified.

Surface	γ[J/m^2]			
	Sn{$5s^2 4d^{10} 5p^2$}, O{$2s^2 2p^5$}, F{$2s^2 2p^5$}		Sn{$5s^2 5p^2$}, O{$2s^2 2p^5$}, F{$2s^2 2p^5$}	
	Clean	F-terminated	Clean	F-terminated
001	1.62	0.54	1.68	0.57
110	0.91	0.13	0.92	0.12
102	1.5	–0.15	1.55	–0.138
113	2.02	0.076	2.07	0.099

pseudopotential sets, which are consistent with previously calculated data for clean (001) and (110) SnO_2 surfaces.[26] This confirms the reliability of the models and methods adopted. In the absence of fluoride termination, (110) surface is the most favorable, consistent with the most frequently reported SnO_2 surfaces.[1d] As shown in Table 1, surface fluorination significantly lowers γ of $(10\bar{2})$ and $(11\bar{3})$ surfaces due to the high Sn–F bonding energy, rendering them most favorable and corroborating our experimental results. Based on the absence of high index facets when using $SnCl_4 \cdot 5H_2O$ precursor, it is thought that residue non-oxidized Sn^{2+} (when using $SnCl_2 \cdot 2H_2O$) is a key factor in facilitating the high index facets formation. Chemically, this may be facilitated by the presence of SnF_2 or Sn_3F_8 species (both formed only in the presence of Sn^{2+}) on SnO_2 surfaces, which must have a different surface force from SnF_4. Coupled with the γ of individual facets, they have direct influence on the aggregation of SnO_2 sheets that resulted in different long-range morphologies, that is, nanoflowers (for Sn^{2+} starting precursor) and hollow spheres (for Sn^{4+} starting precursor).

During the growth process of the hierarchical $(10\bar{2})$-SnO_2 nanoflowers, plate-like, poorly crystalline structures were initially formed, consisting of spherical particles and nanosheets. As shown in **Figure 2**A, nanoparticles are found on the nanosheets in the first 18 h of growth, which gradually disappear after 56 h growth (Figure 2B). This is a likely indication of the dissolution-deposition Ostwald ripening mechanism.[20] HRTEM as presented in Figure 2D shows the oriented alignment of several layers of nanosheets with identical (200) atomic planes, indicating their oriented growth along the [200] direction. This is consistent with the prominent (200) reflection peak as measured by X-ray diffraction (XRD) for $(10\bar{2})$-SnO_2 compared to that of $(11\bar{2})$-SnO_2 (**Figure 3**A). While the undoped SnO_2 hollow spheres show prominent (200) and (211) reflections (Figure 3A),[16] we note that zero-dimensional SnO_2, i.e, nanoparticles, lacks the (200) diffraction peaks, in a way similar to hydrothermally synthesized SnO_2 nanoflowers made in the absence of fluoride source.[9d,18]

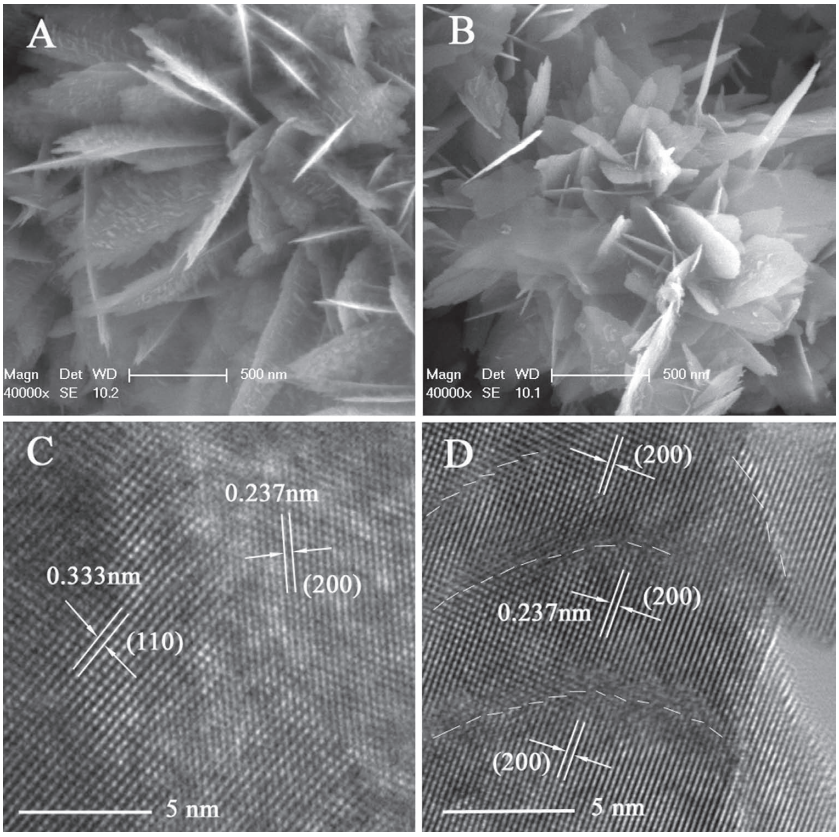

Figure 2. A,B) SEM images of $(10\bar{2})$ faceted SnO_2 nanoflowers obtained at different hydrothermal reaction time: A) 18 and B) 56 h. Also shown are the HRTEM images of C) the boundary areas between SnO_2 nanosheets and attached nanoparticles, and D) growth-oriented nanosheet.

Because Sn^{2+} was used as the precursor, and that not all are oxidized to Sn^{4+}, some residue of the former can in principle be doped in the SnO_2 nanostructures. Indeed, analysis by X-ray photoemission spectroscopy (XPS, Figure 3C) confirms the presence of Sn^{2+} dopants in the resultant SnO_2. This is reflected from the lower Sn $3d_{5/2}$ binding energy compared to the undoped SnO_2 (Sn $3d_{5/2}$: Sn^{4+} = 487.5 eV; Sn^{2+} = 486.5 eV).[30] As shown in Figure 3D, upon doping with Sn^{2+}, the density of states of the O 2p valence band edge extends beyond the intrinsic edge of undoped SnO_2 (curve a). The difference between the conduction (approximated by Fermi level for n-type semiconductor) and valence band edges was measured to be ≈3.64 eV for undoped SnO_2, and 1.55 eV for both doped $(10\bar{2})$-SnO_2 and $(11\bar{3})$-SnO_2. Here, the Sn^{2+} concentration was estimated to be ≈25%, based on the matching of calculated bandgap with induced oxygen vacancies and that measured experimentally. The heavy doping is thought to be possible considering the similarity of Sn^{2+} and Sn^{4+} cations. Sn^{2+}-doping in SnO_2 lattice is a very convenient means of inducing stable oxygen vacancy states and are formed for every substitutional doping of Sn^{2+} in place of Sn^{4+} in order to preserve charge neutrality. Unlike foreign ion dopants, the aliovalent self-doping is advantageous in minimizing structural defects given small difference in ionic radius (hexacoordinated Sn^{4+}: 0.69 Å;[27] hexacoordinated Sn^{2+}: 0.62 Å[28]). As shown in Figure 3B, both doped $(10\bar{2})$-SnO_2 (spectrum b) and doped $(11\bar{3})$-SnO_2 (spectrum c) exhibit extended optical absorption beyond the intrinsic bandgap of undoped SnO_2 (spectrum a) as defined by the band edge absorption threshold of 347 nm (E_g = 3.6 eV). The absorption of ochre-brown doped-SnO_2 powders extends into the infrared regime (>1200 nm), a typical characteristic of oxygen vacancy bandgap states, which normally distribute below the conduction band edge.[29]

To gain more insights on the electronic origin of the optical properties of doped SnO_2, we performed ab initio calculations of the band structures of the undoped and Sn^{2+}-doped SnO_2 based on DFT.[23] Analysis of the total and projected density

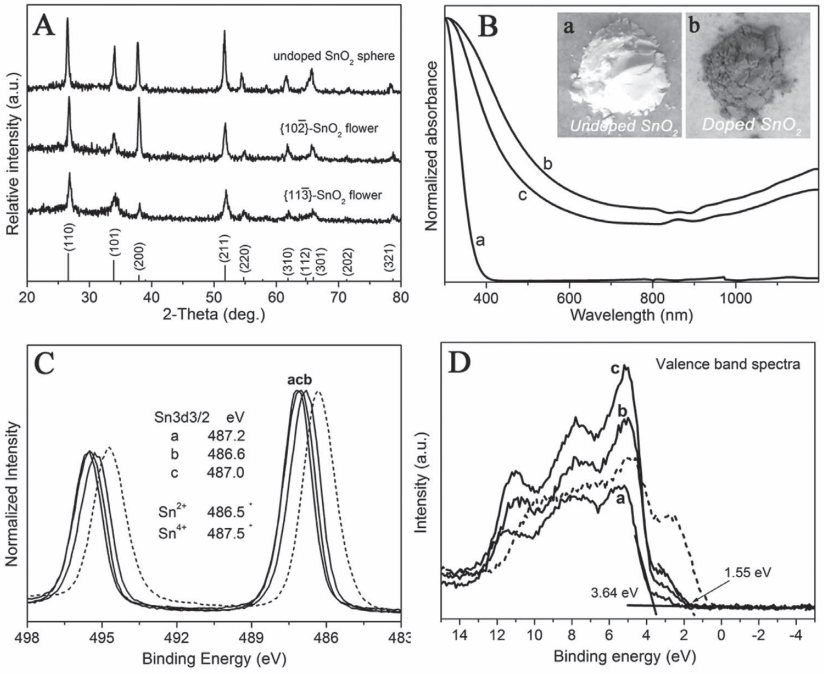

Figure 3. A) X-ray diffraction patterns of undoped SnO_2 hollow spheres and (11$\bar{3}$) and (10$\bar{2}$) faceted SnO_2 nanoflowers. All the diffraction peaks in Figure 3A can be indexed to tetragonal SnO_2 (JCPDS No. 41-1445, P42/mnm). B) UV-visible-NIR diffuse reflectance spectra of (a) undoped SnO_2, (b) (10$\bar{2}$)-SnO_2 nanoflowers and (c) (11$\bar{3}$)-SnO_2 nanoflowers, with inset showing the digital photographs of undoped SnO_2 and Sn^{2+}-doped SnO_2 powders. Also shown are the corresponding C) XPS Sn 3d lines and D) valence band XPS spectra. The dashed lines in panels (C and D) show the XPS Sn 3d lines and the valence spectrum of the (10$\bar{2}$)-SnO_2 nanoflowers after Ar^+ sputtering. All the binding energies are referenced to the C 1s peak at 284.7 eV.

of states of SnO_2 without oxygen vacancy defects (Sn:O = 0.5) shows that the valence states are derived predominantly from the O 2p orbitals, while the conduction states originate from the Sn 5s and O 2p orbitals (**Figure 4**A,B).[31] With the introduction of Sn^{2+} and accompanying oxygen vacancies (shown in Figure 4A for Sn:O = 0.571 and 0.8), the contributions of O 2p, and Sn 5s and 5p orbitals become prominent in both valence and conduction bands (Figure 4A,C). Hybridization of these orbitals further contributes to the bandgap states and extended absorption as corroborated by optical measurements (Figure 3B). The orientations of the highest occupied states on O atoms are wiggled upon the introduction of oxygen vacancies, resulting in the non-uniform states distribution between O atoms at non-equal sites (Figure 4C). Such a state distribution allows efficient trapping of holes carrier on O atoms.[3c]

When heavily doped with Sn^{2+} (Sn:O ≥ 0.8), bridging of conduction and valence band states in an otherwise forbidden gap is possible (Figure 4A). This is verified experimentally through the exaggeration of Sn^{2+} content by Ar^+ ionization-sputtering of doped (10$\bar{2}$)-SnO_2 within the ultrahigh vacuum chamber. The XPS measurement (Figure 3C, dashed line) confirms the extension of O 2p valence band edge position with an extremely narrow gap of 0.6 eV (Figure 3D). Concomitantly, the extended bandgap states result in the gradual shifting of intrinsic Fermi level E_i to the higher energy states (Figure 4A). It is interesting to note that the higher level of delocalized states points to the higher electrical conductivity. It has long been thought that increased oxygen vacancies, such as that induced here by Sn^{2+} self-doping, gives rise to shallow donor levels near the conduction band, which in turn enhanced conductivity.[32]

As proof-of-concept, we demonstrate the application of the doped SnO_2 nanoflowers for chemiresistive gas sensing. Specific exposed high energy facets are known to influence the adsorption geometry of an analyte molecule and subsequently its gas sensing response.[33] As evident from **Figure 5**A, the (10$\bar{2}$)-SnO_2 exhibits an order of magnitude higher in sensing response of NO_2, compared to undoped SnO_2. This is true despite the lower specific surface area of the former (21 m^2 g^{-1} vs 35 m^2 g^{-1} for undoped SnO_2). The same applies to (11$\bar{3}$)-SnO_2 (67 m^2 g^{-1}) although it is only 65% of the response of (10$\bar{2}$)-SnO_2 at 33 ppm NO_2. The mechanism of NO_2 sensing as an oxidizing gas can be described by its chemisorption on SnO_2 followed by interfacial electron transfer: NO_2 (g) + e^- ⇔ NO_2^- (ad). Note that the sensing response versus concentration is in strict conformation with the expected power law dependency. While oxygen vacancies on SnO_2 surface are known to be the active sites for NO_2 chemisorption and subsequent charge transfer,[34] the difference in sensing response between (10$\bar{3}$)- and (11$\bar{3}$)-SnO_2 facets reflects the efficacy of interfacial charge transfer between them and the NO_2 gas as discussed below.

As shown in **Figure 6**, NO_2 preferentially adsorbs onto unsaturated Sn surface atoms adjacent to the oxygen vacancy, resulting in the appearance of a new mid-bandgap energy level upon adsorption of NO_2, which is located closer to the conduction band minimum for SnO_2-(10$\bar{2}$) than for (11$\bar{3}$) surface (Figure 6B,D). Furthermore, the charge distribution at Γ point (*cd2*) for the former is delocalized on the surface. As reported by Maiti and coworkers, the shift of Fermi levels towards higher energies in doped-SnO_2 compared to undoped SnO_2 (Figure 4A) is beneficial in enhancing the electron injection efficiencies from the valence band maximum to NO_2 adsorbate.[34b] In particular, our Bader charge analyses found preferential electron transfer from the surface Sn atoms adjacent to an oxygen vacancy to the half-occupied HOMO of the NO_2 adsorbate.[35] More relevantly, the charge transfer potential from doped SnO_2-(10$\bar{2}$) to NO_2 was found to be greater than that from (11$\bar{3}$) surface. All these factors point to the more favorable interfacial charge transfer between NO_2 and doped SnO_2-(10$\bar{2}$), as well as the corresponding changes in conductance, i.e., chemiresistive sensing. Compared to NO_2, the doped-SnO_2 sensors show high selectivity, with essentially low responses towards volatile organic carbons such as acetone (Figure 5B) and ethanol (Figure 5C).

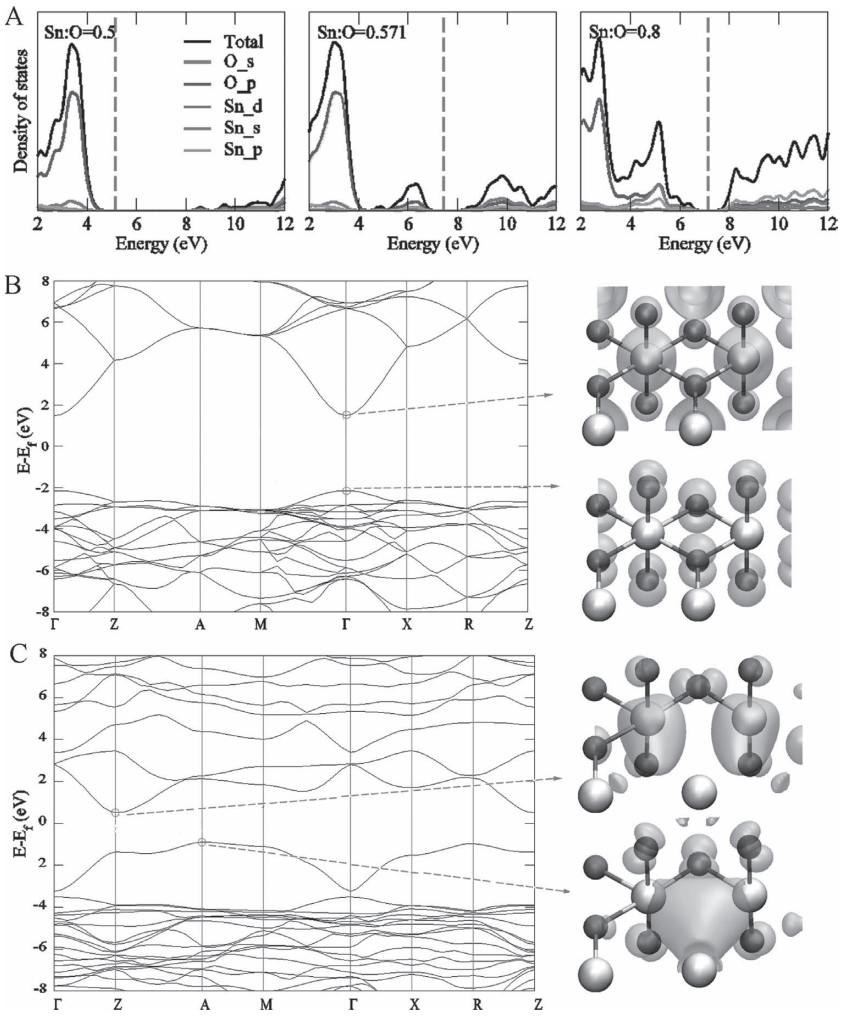

Figure 4. A) Calculated density of states of undoped SnO_2 and Sn^{2+}-doped SnO_2 with different concentrations of oxygen vacancies (the dashed lines indicate the position of the Fermi level). B,C) Band structures of undoped SnO_2 and Sn^{2+}-doped SnO_2 with Sn:O = 0.571, respectively. Shown in blue on the right hand side are the corresponding distributions of states at the conduction band minimum and the valence band maximum, with O and Sn atoms represented by the red and white spheres, respectively.

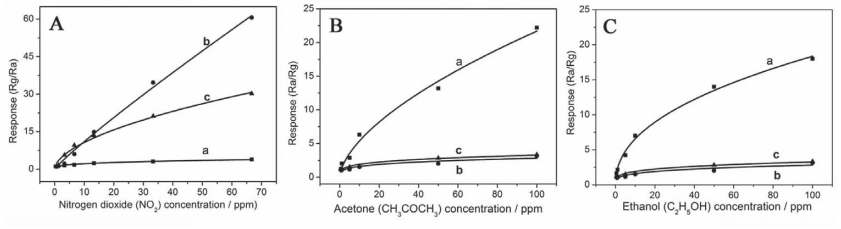

Figure 5. Sensitivity of undoped SnO_2 (a), as well as $(10\bar{2})$-SnO_2 (b) and $(11\bar{3})$-SnO_2 (c) nanoflowers towards A) oxidizing gas nitrogen dioxide, as well as non-oxidizing vapors B) acetone and C) ethanol. In all cases, the sensing response versus concentration are in strict conformation with the power law dependence.[38,39]

3. Conclusions

We showcase the synthesis of hierarchical Sn^{2+}-doped SnO_2 nanoflowers with tunable predominant $(10\bar{2})$ and $(11\bar{3})$ facets, with exciting optical, electronic and sensing properties. In terms of materials design, our synthetic approach combines in a simultaneous fashion, three desirable fundamental materials properties namely, shape and facets design, oxygen vacancy and band structure engineering. The facet-dependent gas sensing of these nanostructures was demonstrated, with $(10\bar{2})$- and $(11\bar{3})$-faceted SnO_2 nanoflowers showing high NO_2 gas sensing sensitivity and selectivity. This was attributable to the more favorable interfacial charge transfer between NO_2 and doped-SnO_2 surfaces. Our synthetic strategy towards hierarchical SnO_2 nanostructures with specific exposed crystal facets not only points a way to improve the sensitivity and selectivity of SnO_2-based sensors, but is also important for exploitation of other intrinsic facet-dependent properties of this wide-bandgap metal oxide, related to its use in lithium ion batteries, solar cells, and catalysis. The combination of novel properties demonstrated here allows the fundamental extension of SnO_2 applications in various technological advances, especially where enhanced or tunable charge transfer is concerned.

4. Experimental Section

Materials Preparation: All chemicals, including tin(II) chloride dihydrate ($SnCl_2{\cdot}2H_2O$, analytical reagent grade, Tianjin, China), and sodium fluoride (NaF, Sigma-Aldrich), were used as received without any further treatment. In a typical synthesis, $SnCl_2{\cdot}2H_2O$ (2.85 mmol, 0.64 g) and certain amount of NaF were dissolved in distilled water (30 mL) and produced a clear precursor solution after stirring for 30 min, as NaF at $R_{F/Sn} \geq 3$ inhibits the fast hydrolysis of $SnCl_2{\cdot}2H_2O$. By varying the amount of NaF, $(11\bar{3})$-SnO_2 and $(10\bar{2})$-SnO_2 nanoflowers have been obtained for $R_{F/Sn}$ equal to 3 and 4.8, respectively, by hydrothermal treatment. Undoped SnO_2 microspheres were prepared by hydrothermally treating the precursor solution consisting of $SnCl_4{\cdot}5H_2O$ (2.85 mmol, 1.0 g) and NaF ($R_{F/Sn}$ = 4.8), which were dissolved in 30 mL distilled water and produced a clear solution after stirring for 30 min. All the hydrothermal reactions were performed by keeping the Teflon-lined stainless steel autoclaves in an electric oven at 180 °C for 24 h. Products were collected and washed with distilled water employing several centrifugation cycles, followed by drying at 90 °C overnight.

Characterization: Powder X-ray diffraction (XRD) patterns were taken on a Philips X'Pert X-ray diffractometer using Cu Kα radiation (λ = 1.5418 Å). Scanning electron microscopy (SEM) and transmission electron microscopy (TEM) were performed on a Philips XL30 FEG SEM and JEOL JEM2100F TEM, respectively. Specific surface area of the samples was estimated using Brunauer-Emmett-Teller (BET) method on a NOVA 1200e Surface Area and Pore Size Analyzer (Quantachrome Instruments). UV-visible-NIR diffuse reflectance spectra

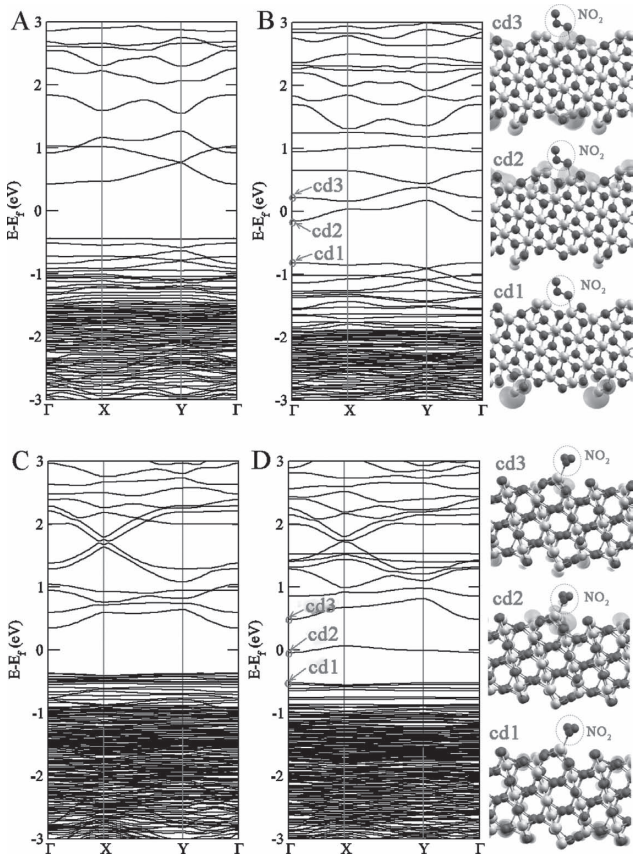

Figure 6. Band structures of the A,B) oxygen vacancy doped $(10\bar{2})$-SnO_2 surface as well as the C,D) oxygen vacancy doped $(11\bar{3})$-SnO_2 surface without (A,C) and with (B,D) NO_2 adsorption on an unsaturated three-fold-coordinated Sn atom. The corresponding charge distributions *cd1*, *cd2* and *cd3* indicated in the band structures at the Γ point are presented on the right. The N, O and Sn atoms are represented by the blue, red and white spheres, respectively.

(DRS) were measured with a UV-vis-NIR spectrophotometer (Shimadzu UV-3600). X-ray photoelectron spectroscopy (XPS, Physical electronics PHI-5802) was applied to determine the surface composition of the products. In order to enlarge the signals of Sn^{2+} in the XPS spectra, higher doses of argon ions (Ar^+) were used to sputter away a layer of 20 nm of the samples to produce a pure layer of Sn^{2+} through reducing Sn^{4+} by Ar^+. All the binding energies were calibrated with the reference C 1s peak at 284.7 eV from the surface adventitious carbon.

Gas Sensing Study: A paste composed of the SnO_2 nanoparticles was uniformly coated onto an alumina tube with previously printed Au electrodes and Pt wires, followed by sintering at 400 °C for 2 h in a muffle furnace. After a Ni-Cr heating wire was inserted, all of the six wires were welded onto the substrate, followed by aging of sensors at 350 °C for 240 h in air. All the gas measurements were performed on a testing system HW-30A (Hanwei Electronics Co. Ltd., P.R. China). Testing gases were injected into a glass chamber and mixed with air (air humidity: 47%). A stationary state gas distribution method was used for testing the gas response. All sensing experiments were performed at constant temperature (25.0 ± 1.0 °C). The sensor gas response (sensitivity S) in this paper is defined as $S = R_a/R_g$ for oxidizing gases and $S = R_g/R_a$ for volatile organic vapors, where R_a and R_g are the resistance in air and in the testing gas, respectively. The response time or recovery time was defined as the time taken for the sensor output to reach 90% of its saturation value after applying or switching off the gas as a step function.

DFT Calculations: The density functional theory calculations were carried out for the electronic structures of perfect and oxygen-vacancy containing tin dioxide by employing the VASP package.[23] The band structure calculations of bulk SnO_2 were performed using the planewave projector augmented-wave (PAW) method[36] with Heyd-Scuseria-Ernzerhof (HSE) hybrid functional as implemented in the VASP code.[23c,36] The screening parameter in HSE was fixed at a value of 0.2 $Å^{-1}$.[36] The fraction of the nonlocal exchange was fixed at a = 0.32. The Sn 4d electrons were treated explicitly as valence electrons. The cutoff energy for the plane wave basis was 350 eV. All atoms were relaxed until the Hellmann-Feynman forces acting on them were below 0.02 eV/Å. The electronic properties of NO_2 adsorption on SnO_2 as shown in Figure 6 of this article were performed using generalized gradient approximation (GGA) PBE functional.[37] The Sn 4d electrons were not treated as valence electrons in this part.

For surface free energy calculations, stoichiometric slab models (1 × 1) were employed to simulate the surface; each cell consisted of 27 atoms, 30 atoms, 39 atoms and 60 atoms for clean (001), (110), $(10\bar{2})$ and $(11\bar{3})$ surfaces, respectively. The thickness of each slab was set as 10 Å and the vacuum space between slabs as larger than 15 Å. Based on previous related studies,[2b] γ was calculated according to the following equation:

$$\gamma = \frac{E_{slab} - N E^{Sno_2}_{bulk} - N_F E_F}{2A}$$

Here, the $E^{Sno_2}{}_{bulk}$ is the energy per SnO_2 unit of bulk SnO_2, the E_{slab} is the total energy of the slab in the unit cell, the N is the total number of SnO_2 units contained in the slab model, N_F is the number of adsorbed fluorine atoms, $E_F = \frac{1}{2} E_{F_2}$, where E_{F_2} indicates the total energy of F_2, and the A is the area of one slab surface in the unit cell.

Acknowledgements

H.K.W. and K.P.D. contributed equally to this work. This work was supported by the Applied Research Grant 9667067 of City University of Hong Kong, and through the Centre for Functional Photonics.

Received: January 25, 2013
Revised: February 20, 2013
Published online: April 9, 2013

[1] a) G. A. Somorjai, *Chem. Rev.* **1996**, *96*, 1223; b) F. Seker, K. Meeker, T. F. Kuech, A. B. Ellis, *Chem. Rev.* **2000**, *100*, 2505; c) M. Kiskinova, *Chem. Rev.* **1996**, *96*, 1431; d) M. Batzill, K. Katsiev, J. M. Burst, U. Diebold, A. M. Chaka, B. Delley, *Phys. Rev. B* **2005**, *72*, 165414.
[2] a) N. Tian, Z.-Y. Zhou, S.-G. Sun, Y. Ding, Z. L. Wang, *Science* **2007**, *316*, 732; b) H. G. Yang, C. H. Sun, S. Z. Qiao, J. Zou, G. Liu, S. C. Smith, H. M. Cheng, G. Q. Lu, *Nature* **2008**, *453*, 638; c) S. W. Liu, J. G. Yu, M. Jaroniec, *J. Am. Chem. Soc.* **2010**, *132*, 11914; d) X. Han, Q. Kuang, M. Jin, Z. Xie, L. Zheng, *J. Am. Chem. Soc.* **2009**, *131*, 3152.
[3] a) J. Wang, D. N. Tafen, J. P. Lewis, Z. Hong, A. Manivannan, M. Zhi, M. Li, N. Wu, *J. Am. Chem. Soc.* **2009**, *131*, 12290; b) F. Zuo, L. Wang, T. Wu, Z. Zhang, D. Borchardt, P. Feng, *J. Am. Chem. Soc.* **2010**, *132*, 11856; c) X. Chen, L. Liu, P. Y. Yu, S. S. Mao, *Science* **2011**, *331*, 746; d) G. Liu, H. G. Yang, X. W. Wang, L. N. Cheng, J. Pan, G. Q. Lu, H. M. Cheng, *J. Am. Chem. Soc.* **2009**, *131*, 12868.
[4] R. Yang, W. Zhao, J. Zheng, X. Z. Zhang, X. G. Li, *J. Phys. Chem. C* **2010**, *114*, 20272.
[5] L. Vayssieres, M. Graetzel, *Angew. Chem. Int. Ed.* **2004**, *43*, 3666.
[6] Y. Wang, X. Jiang, Y. Xia, *J. Am. Chem. Soc.* **2003**, *125*, 16176.
[7] Q. Kuang, T. Xu, Z.-X. Xie, S.-C. Lin, R.-B. Huang, L.-S. Zheng, *J. Mater. Chem.* **2009**, *19*, 1019.

[8] C. Wang, Y. Zhou, M. Ge, X. Xu, Z. Zhang, J. Z. Jiang, *J. Am. Chem. Soc.* **2009**, *132*, 46.
[9] a) J. Zhang, X. H. Liu, S. H. Wu, M. J. Xu, X. Z. Guo, S. R. Wang, *J. Mater. Chem.* **2010**, *20*, 6453; b) D. Deng, J. Y. Lee, *Chem. Mater.* **2008**, *20*, 1841; c) R. Demir-Cakan, Y. S. Hu, M. Antonietti, J. Maier, M. M. Titirici, *Chem. Mater.* **2008**, *20*, 1227; d) H. B. Wu, J. S. Chen, X. W. Lou, H. H. Hng, *J. Phys. Chem. C* **2011**, *115*, 24605.
[10] a) K. Ariga, Q. Ji, M. J. McShane, Y. M. Lvov, A. Vinu, J. P. Hill, *Chem. Mater.* **2011**, *24*, 728; b) *Insights into Hierarchically Structured Porous Materials: From Nanoscience to Catalysis, Separation, Optics, Energy, and Life Science* (Eds: B.-L. Su, C. Sanchez, X.-Y. Yang), Wiley-VCH, Weinheim, Germany **2011**.
[11] R. W. J. Scott, Ph.D. Thesis, University of Toronto **2002**.
[12] H. G. Yang, G. Liu, S. Z. Qiao, C. H. Sun, Y. G. Jin, S. C. Smith, J. Zou, H. M. Cheng, G. Q. Lu, *J. Am. Chem. Soc.* **2009**, *131*, 4078.
[13] X. Han, M. Jin, S. Xie, Q. Kuang, Z. Jiang, Y. Jiang, Z. Xie, L. Zheng, *Angew. Chem. Int. Ed.* **2009**, *48*, 9180.
[14] a) M. Liu, L. Y. Piao, W. M. Lu, S. T. Ju, L. Zhao, C. L. Zhou, H. L. Li, W. J. Wang, *Nanoscale* **2010**, *2*, 1115; b) M. Liu, L. Y. Piao, L. Zhao, S. T. Ju, Z. J. Yan, T. He, C. L. Zhou, W. J. Wang, *Chem. Commun.* **2010**, *46*, 1664; c) J. Y. Feng, M. C. Yin, Z. Q. Wang, S. C. Yan, L. J. Wan, Z. S. Li, Z. G. Zou, *CrystEngComm* **2010**, *12*, 3425.
[15] J. H. Lee, *Sens. Actuators, B* **2009**, *140*, 319.
[16] H. Wang, F. Fu, F. Zhang, H.-E. Wang, S. V. Kershaw, J. Xu, S.-G. Sun, A. L. Rogach, *J. Mater. Chem.* **2012**, *22*, 2140.
[17] *Chemistry of the Elements* (Eds: N. E. Greenwood, A. Earnshaw), 2nd ed., Butterworth-Heinemann, Oxford **1997**.
[18] R. Yang, Y. G. Gu, Y. Q. Li, J. Zheng, X. G. Li, *Acta Mater.* **2010**, *58*, 866.
[19] *Surface Area and Porosity Determinations by Physisorption: Measurements and Theory* (Ed: J. B. Condon), Elsevier Science, Harriman, TN **2006**.
[20] H. K. Wang, W. Shao, F. Gu, L. Zhang, M. K. Lu, C. Z. Li, *Inorg. Chem.* **2009**, *48*, 9732.
[21] a) Y. Sun, Y. Xia, *Science* **2002**, *298*, 2176; b) G. Zhang, X. Lu, W. Wang, X. Li, *Chem. Mater.* **2007**, *19*, 5207; c) C. J. Murphy, *Science* **2002**, *298*, 2139.
[22] a) A. Beltran, J. Andres, E. Longo, E. R. Leite, *Appl. Phys. Lett.* **2003**, *83*, 635; b) D. G. Stroppa, L. A. Montoro, A. Beltran, T. G. Conti, R. O. da Silva, J. Andres, E. R. Leite, A. J. Ramirez, *Chem. Commun.* **2011**, *47*, 3117.
[23] a) G. Kresse, J. Furthmüller, *Phys. Rev. B* **1996**, *54*, 11169; b) G. Kresse, J. Hafner, *Phys. Rev. B* **1993**, *48*, 13115; c) G. Kres, D. Joubert, *Phys. Rev. B* **1999**, *59*, 1758.
[24] G. Kresse, J. Furthmüller, *Comput. Mater. Sci.* **1996**, *6*, 15.
[25] J. P. Perdew, K. Burke, M. Ernzerhof, *Phys. Rev. Lett.* **1996**, *77*, 3865.
[26] a) J. D. Prades, A. Cirera, J. R. Morante, *J. Electrochem. Soc.* **2007**, *154*, H675; b) J. Oviedo, M. J. Gillan, *Surf. Sci.* **2001**, *490*, 221.
[27] R. Shannon, *Acta Crystallogra., Sect. A* **1976**, *32*, 751.
[28] J. Kielland, *J. Am. Chem. Soc.* **1937**, *59*, 1675.
[29] N. Serpone, *J. Phys. Chem. B* **2006**, *110*, 24287.
[30] a) S. Yuan, S. S. Wu, L. Y. Shi, Y. Zhao, J. H. Fang, *J. Colloid Interface Sci.* **2010**, *346*, 12; b) H.-J. Ahn, H.-C. Choi, K.-W. Park, S.-B. Kim, Y.-E. Sung, *J. Phys. Chem. B* **2004**, *108*, 9815.
[31] S. Munnix, M. Schmeits, *Phys. Rev. B* **1983**, *27*, 7624.
[32] a) S. Samson, C. G. Fonstad, *J.Appl. Phys.* **1973**, *44*, 4618; b) Z. M. Jarzebski, J. P. Marton, *J. Electrochem. Soc.* **1976**, *123*, 199C.
[33] G. Liu, J. C. Yu, G. Q. Lu, H.-M. Cheng, *Chem. Commun.* **2011**, *47*, 6763.
[34] a) M. Epifani, J. D. Prades, E. Comini, E. Pellicer, M. Avella, P. Siciliano, G. Faglia, A. Cirera, R. Scotti, F. Morazzoni, J. R. Morante, *J. Phys. Chem. C* **2008**, *112*, 19540; b) A. Maiti, J. A. Rodriguez, M. Law, P. Kung, J. R. McKinney, P. Yang, *Nano Lett.* **2003**, *3*, 1025.
[35] a) G. Henkelman, A. Arnaldsson, H. Jónsson, *Comput. Mater. Sci.* **2006**, *36*, 354; b) E. Sanville, S. D. Kenny, R. Smith, G. Henkelman, *J. Comput. Chem.* **2007**, *28*, 899; c) W. Tang, E. Sanville, G. Henkelman, *J. Phys.: Condens. Matter* **2009**, *21*, 084204.
[36] a) P. E. Blöchl, *Phys. Rev. B* **1994**, *50*, 17953; b) J. Heyd, G. E. Scuseria, M. Ernzerhof, *J. Chem. Phys.* **2006**, *124*, 219906.
[37] J. P. Perdew, K. Burke, M. Ernzerhof, *Phys. Rev. Lett.* **1996**, *77*, 3865.
[38] N. Barsan, U. Weimar, *J. Electroceram.* **2001**, *7*, 143–167.
[39] M. E. Franke, T. J. Koplin, U. Simon, *Small* **2006**, *2*, 36.